Phase transformation and age-hardening of hexagonal α′ martensite in Ti–12 mass%V–2 mass%Al alloys studied by transmission electron microscopy

Kazuhisa Sato [a,*], Hiroaki Matsumoto [a], Kazuki Kodaira [b], Toyohiko J. Konno [a], Akihiko Chiba [a]

[a] Institute for Materials Research, Tohoku University, 2-1-1 Katahira, Aoba, Sendai 980-8577, Japan
[b] Department of Materials Science, Tohoku University, 6-6 Aoba, Sendai 980-8579, Japan

ARTICLE INFO

ABSTRACT

Microstructure and phase decomposition of α′ martensites in Ti–12 mass%V–2 mass%Al alloys have been studied by transmission electron microscopy (TEM) and scanning transmission electron microscopy (STEM). The as-quenched alloy showed an acicular structure of the hexagonal α′ martensite. Significant age-hardening was observed in the alloys after aging at 300 and 400 °C. A hardness, as high as 377 Hv, was obtained for the alloy after aging at 400 °C for 24 h. The age-hardening can be attributed to fine β precipitates nucleated inside primary α′-martensite plates. These fine acicular precipitates, about 50 nm in length, were identified using high-angle annular dark-field (HAADF) STEM as bright contrasts, indicating a vanadium-rich composition of the β precipitates. As the aging temperature increases, partitioning of vanadium becomes prominent, indicating phase decomposition towards the equilibrium α and β phases. Decomposition of the α′ martensite and formation of α/β two-phase structure were observed after aging at 500 °C for 24 h, which resulted in an abrupt decay of hardness. Plate-like three-dimensional shapes of large β precipitates have been revealed by HAADF-STEM electron tomography.

© 2010 Elsevier B.V. All rights reserved.

1. Introduction

Titanium alloys are widely used in various fields, such as aerospace and automobile industries, and biomedical applications [1–3], due to their high specific strength and corrosion resistance. Among the Ti-alloy systems, Ti–V alloys composed of hexagonal α′ martensites possess low Young's moduli (∼60 GPa) and high strength (∼1000 MPa), and show a good machinability for cold groove rolling [4–7]. Recent studies on α′-type Ti–V–Al alloys revealed the increase of Young's modulus and Vickers hardness by aging at 300–400 °C [6,7]. Age-hardening was previously reported for binary Ti–V alloys with a V content of 12.5–20% [8–10], which has been attributed to spinodal decomposition of the orthorhombic α″ martensite [10]. In contrast, age-hardening was reported to take place only insignificantly for Ti–V alloys with the hexagonal α′ martensite [10]. In a similar Ti–Mo system, age-hardening has also been reported to occur, where two mechanisms for the hardening have been clarified [11]: one is spinodal decomposition of the α″ martensite for the alloys with a Mo content of 4–8 mass%, and the other is homogeneous precipitation of the β phase within α′ crystals for a 3 mass%Mo alloy aged below 575 °C. The latter alloy with a small amount of α′ martensites showed insignificant age-hardening when heterogeneous precipitation occurs by

aging above 575 °C. The phase separation behavior is associated by decomposition of martensite supersaturated with solute V or Mo towards the equilibrium hexagonal α and cubic β phases in the Ti–V and Ti–Mo systems [12,13]. Besides a consideration from the viewpoint of phase diagrams, electronic structure calculation has also indicated tendencies of phase separation in the Ti–V system [14].

In the binary Ti–V system, two kinds of martensite phases can be formed by quenching a high-temperature solid solution (β phase) with a body centered cubic (bcc) structure, depending on the solute V content: when it is higher than 9.4 mass%, the orthorhombic α″ martensitic phase is formed [1], whereas below this value the hexagonal α′ martensitic phase is formed. An addition of a small amount of Al (2 mass% in this study) leads to suppression of the formation of the athermal ω phase as well as to stabilization of the hexagonal α phase. In addition, alloying of Al stabilizes the α′ martensite. Accordingly, X-ray diffraction (XRD) patterns of Ti–12%V–2%Al alloys aged at 300 °C or 400 °C, as well as those of the as-quenched alloy after solution treatment (hereafter, STQ), exhibit no reflections of the equilibrium α or β phases, i.e., the α′ martensite phase is maintained. Hence, in spite of recent findings of high strength and cold workability of ternary α′-type Ti–V–Al alloys, the origin of age-hardening in this alloy system still remains an open question.

In the present study, microstructure composed of α′ martensites in Ti–12 mass%V–2 mass%Al alloys and its decomposition behaviors upon aging were studied by aberration-corrected (AC)

* Corresponding author. Tel.: +81 22 215 2629; fax: +81 22 215 2126.
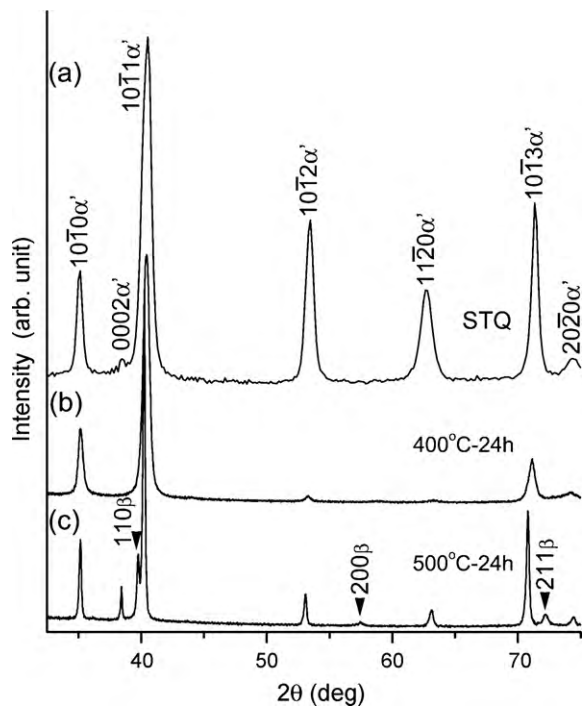E-mail address: ksato@imr.tohoku.ac.jp (K. Sato).

Fig. 1. XRD profiles of Ti–12 mass%V–2 mass%Al alloys. (a) Solution treated and quenched (STQ), (b) after aging at 400 °C for 24 h, and (c) after aging at 500 °C for 24 h. Reflections of the β phase are indicated by arrowheads in Fig. 1c.

high-resolution transmission electron microscopy (HRTEM) and high-angle annular dark-field scanning transmission electron microscopy (HAADF-STEM). In addition to highly improved spatial resolution, AC-HRTEM benefits from smaller defocus values under optimal defocus conditions due to small spherical aberration (C_s) values, which enables unambiguous identification of interface structures free from contrast delocalization. Chemically sensitive atomic number (Z) contrast of HAADF-STEM was used to observe decomposition of α′ martensites on aging associated with a compositional variation. We also examined three-dimensional (3D) structures of β precipitates by means of electron tomography using HAADF-STEM. Z contrast can be regarded as a mass-thickness contrast required for electron tomography, where incoherent imaging is dominant and artifacts from diffraction contrasts are minimum.

2. Experimental procedure

Ti–12 mass%V–2 mass%Al alloys were prepared by arc melting in an argon atmosphere using high purity Ti, V, and Al, followed by homogenization at 1150 °C for 24 h. The homogenized buttons were solution treated at 950 °C (above the β transus) for 2 h in an evacuated quartz tube, and then quenched into ice water (STQ). Aging conditions for the quenched alloys were 300, 400, and 500 °C for 0.5–500 h (3 weeks). Chemical analysis for the STQ alloy showed carbon, nitrogen and oxygen contents be 0.025 mass% C, 0.009 mass% N and 0.104 mass% O, respectively [15]. Phase identification was carried out by means of XRD using a Panalytical X'pert MPD diffractometer with a Cu-Kα_1 radiation. Microstructures of these alloys were studied using a JEOL JEM-2000FX TEM operating at 200 kV. HRTEM and STEM images were obtained using an FEI Titan 80-300 (S)TEM operating at 300 kV with a field emission gun and a CEOS image corrector. We adopted a negative third-order spherical aberration (typically, $C_s = -1 \mu m$) with a slightly overfocus condition for the HRTEM observation. All HRTEM images were recorded by a 1 k × 1 k charge coupled device (CCD) camera. HRTEM images were simulated using the MACTEMPAS software, which is based on the multislice method. HAADF-STEM images were acquired using a HAADF detector (Fischione model 3000) with a detector inner angle (half angle) greater than 60 mrad. Elemental analyses were carried out using an energy dispersive X-ray spectrometer (EDS) attached to the 300 kV-(S)TEM. A single-tilt holder (Fischione model 2020) was used for tilt-series acquisition with the maximum tilt angle of 70°. We used an FEI Inspect3D software package for subsequent data processing, including alignment of the tilt axis for the obtained data set based on an iterative cross-correlation
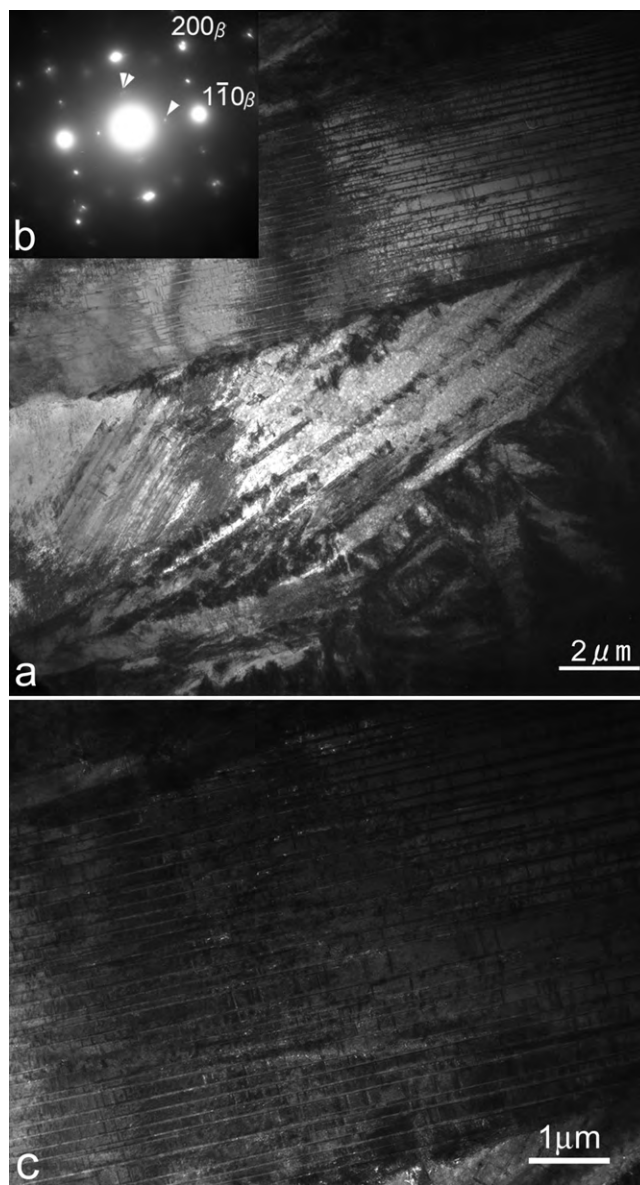

Fig. 2. Microstructure of the STQ Ti–12 mass%V–2 mass%Al alloy. (a) BF-TEM image and (b) corresponding SAED pattern with the beam incidence of $[0\,0\,1]_\beta$, or equivalently $[\bar{1}\,2\,\bar{1}\,0]_{\alpha'}$. The single- and double-arrowheads indicate the existence of two variants of the hexagonal α′ martensite. (c) DF-TEM image taken with $1\,\bar{1}\,0_\beta$ reflection.

technique, and 3D reconstruction. As for the algorithm for 3D reconstruction, we employed weighted back-projection (WBP) method [16]. The reconstructed 3D density data were then visualized using the AMIRA 4.1 software (VISAGE IMAGING).

3. Results and discussion

3.1. Microstructure of the α′ martensites and their evolution upon age-hardening

Fig. 1 shows XRD profiles of the STQ alloy and of aged alloys. The STQ alloy is composed of hexagonal α′ single phase as shown in Fig. 1a. Also no reflections of the β phase were detected in the alloy after aging at 400 °C for 24 h (Fig. 1b). In contrast, the XRD profile of the alloy after aging at 500 °C for 24 h includes reflections of the β phase in addition to those belong to the hexagonal α′ phase (Fig. 1c). These observations clearly indicate the evolution of phase decomposition of α′ martensite towards the equilibrium α
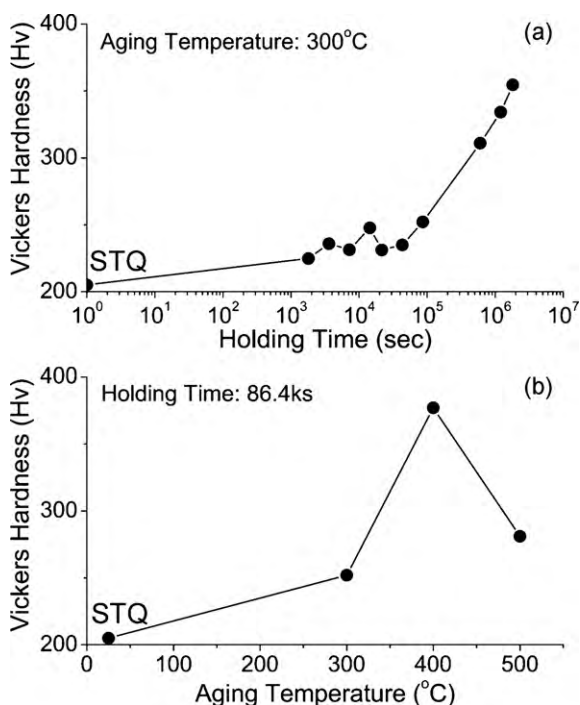
Fig. 3. (a) Increase of Vickers hardness at 300 °C as a function of holding time. Substantial age-hardening can be seen. (b) Vickers hardness as a function of aging temperature (24 h). The hardness, as high as 377 Hv, was observed after aging for 86.4 ks (24 h) at 400 °C.

Fig. 4. Microstructure of Ti–12 mass%V–2 mass%Al alloy after aging at 400 °C for 24 h. (a) SAED pattern with the beam incidence of $[0\,1\,\bar{1}\,1]_{\alpha'}$. Extra reflections due to the $\{1\,0\,\bar{1}\,1\}$-type twins are seen, as indicated by arrowheads. (b) Corresponding BF-TEM image. Thin twin band, 20–50 nm in width, are seen. (c) Aberration-corrected HRTEM image of $\{1\,0\,\bar{1}\,1\}$-type twin boundaries. A magnified image is shown in the inset, where the $(1\,0\,\bar{1}\,1)_{\alpha'}$ plane is clearly seen. Note that the twin boundaries are free from precipitates or extra stacking faults.

and β phases on annealing. To clarify the phase separation behavior precisely, we carried out TEM and STEM observation.

Fig. 2a shows a bright-field (BF) TEM image of the as-quenched alloy viewed along the $[\bar{1}\,2\,\bar{1}\,0]$ axis of the hexagonal α′ martensite phase. An acicular martensite structure with martensite plates, typically a few hundred nanometers in thickness, is seen. These martensite morphologies, composed of large primary martensite plates and many other smaller ones, are similar to those observed in binary Ti–V alloys [5,10,16]. Fig. 2b is a corresponding selected area electron diffraction (SAED) pattern taken from this area. The pattern was taken with the beam incidence of $[0\,0\,1]_{\beta}$. In addition to clear $1\,\bar{1}\,0$ and $2\,0\,0$ reflections of the β phase, a reflection marked by an arrowhead indicates $0\,0\,0\,1_{\alpha'}$ with the beam incidence of $[\bar{1}\,2\,\bar{1}\,0]_{\alpha'}$ of the hexagonal martensite structure. Also a double-arrowhead indicates another $0\,0\,0\,1_{\alpha'}$ reflection from another variant of the α′ martensite with the c-axis orthogonal to the former. It should be mentioned here that the β phase was not detected by XRD (Fig. 1a), and can be considered as a retained phase on quenching. Invisibility of the β phase by XRD suggests that the amount of the retained β phase is quite small. From the SAED pattern, the orientation relationship (OR) between the β and the α′ phases can be deduced as follows:

$$(0\,0\,0\,1)_{\alpha'} \| (1\,\bar{1}\,0)_{\beta},\ [\bar{1}\,2\,\bar{1}\,0]_{\alpha'} \approx \|[0\,0\,1]_{\beta}$$

This OR is quite close to the Burgers' OR $((0\,0\,0\,1)_{\alpha'} \| (1\,\bar{1}\,0)_{\beta},\ [1\,1\,\bar{2}\,0]_{\alpha'} \| [1\,1\,1]_{\beta})$, which is frequently observed between the retained β and the α′ martensite [17–19]. Davis et al. have also reported the retention of thin β layers between the α′ crystals, but no precipitation within the α′ crystal, for as-quenched Ti–2 and 3%Mo alloys [11]. To clarify the morphology of the retained β phase, we observed a dark-field (DF) TEM image using $1\,\bar{1}\,0_{\beta}$ reflection, and found that there exist thin layers between α′ martensite plates as shown in Fig. 2c. Here it should be noted that, in the SAED pattern shown in Fig. 2b, reflections of the β phase almost overlap with weak reflections of the hexagonal
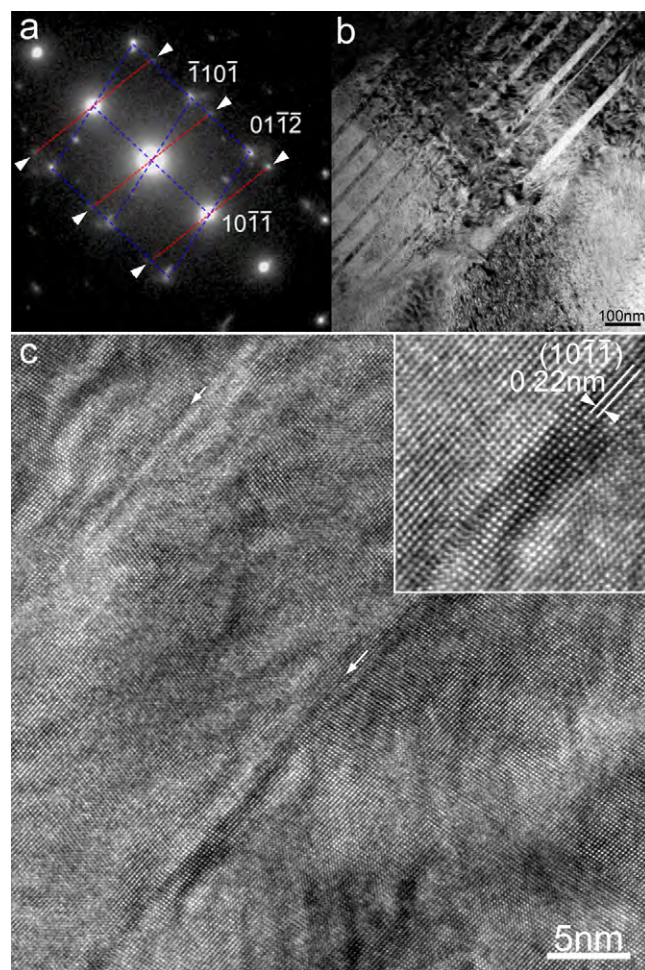
α′ martensite because of the orientation relationship close to the Burgers' one. Therefore, part of the bright contrasts observed in Fig. 2c are not only those arising from the retained β phase but also those from primary α′ crystals.

Fig. 3a shows changes of Vickers hardness as a function of holding time at 300 °C. The initial hardness of the STQ alloy was 205 Hv, and it drastically increased after aging for $\sim 6 \times 10^5$ s (1 week). The hardness reached 355 Hv after aging for $\sim 1.8 \times 10^6$ s (3 weeks). Fig. 3b compares the Vickers hardness obtained at different aging temperatures after aging for 24 h (86.4 ks). The hardness, as high as 377 Hv, was observed for the alloy after aging at 400 °C. As stated earlier, XRD detected no reflections except for those arising from the α′ martensite phase; however, as for the mechanism of the age-hardening, there is a strong possibility of a contribution from fine β precipitates. In a Ti–7.4%V alloy, Flower et al. [10] have reported heterogeneous nucleation of β plates at twin boundaries and on dislocations after aging for 10^4 min at 375 °C, although no significant hardening was observed.

To examine possible formation of a secondary phase at twin boundaries of aged α′ martensites, we have carried out HRTEM observation on twin boundaries for the alloy showing the maximum hardness after aging for 24 h at 400 °C. Fig. 4a and b shows, respectively, SAED pattern with a beam incidence of $[0\,1\,\bar{1}\,1]_{\alpha'}$ and
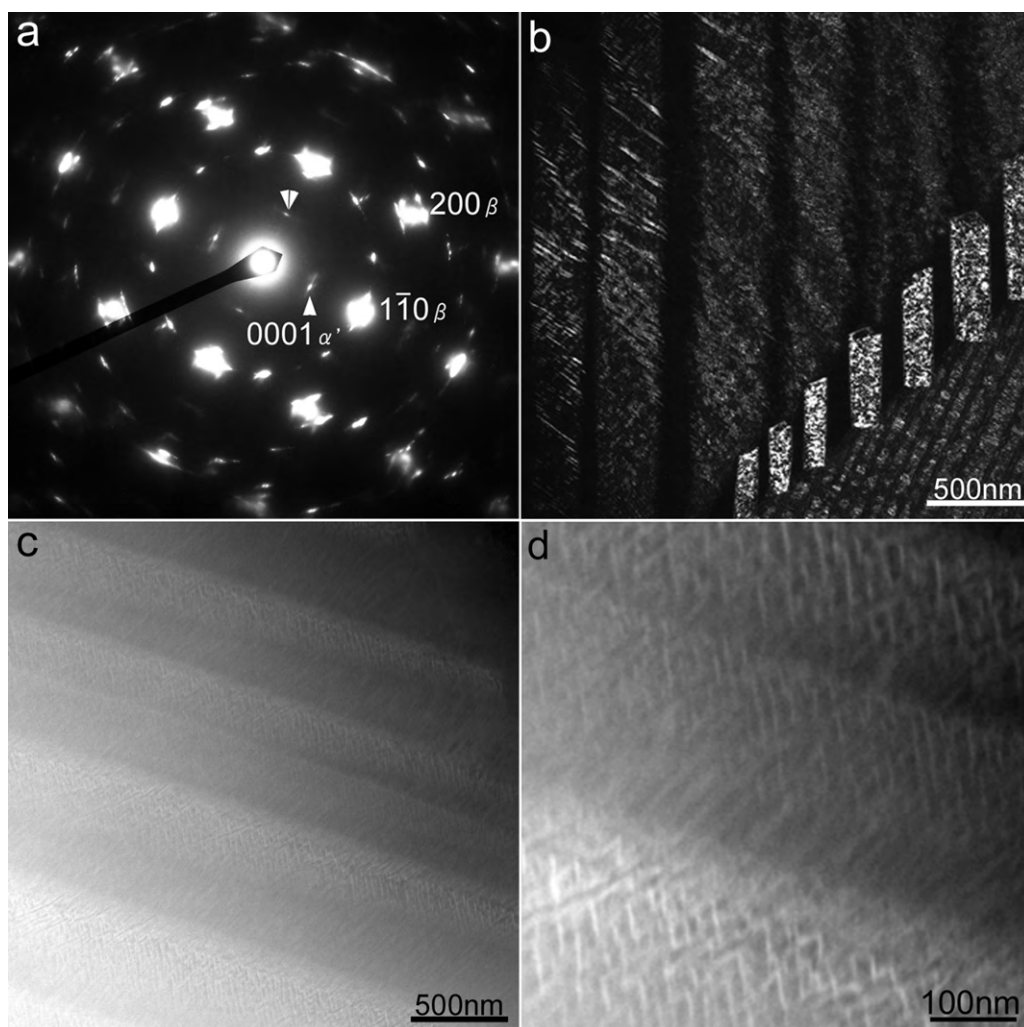
Fig. 5. Microstructure of a Ti–12 mass%V–2 mass%Al alloy after aging at 400 °C for 24 h. (a) SAED pattern with the beam incidence of $[0\,0\,1]_\beta$ or $[\bar{1}\,2\,\bar{1}\,0]_{\alpha'}$. Single- and double-arrowheads indicate $0\,0\,0\,1_{\alpha'}$ reflections belonging to different variants. (b) DF-TEM image taken using $\bar{1}\,1\,0_\beta$ reflection. Fine morphologies inside the aged α' crystals can be seen. (c) HAADF-STEM image, (d) HAADF-STEM image at a higher resolution. Fine acicular precipitates, ~50 nm in length, can clearly be seen as bright contrasts inside the primary α'-plates. Age-hardening observed in this alloy can be attributed to these high-density fine β precipitates inside the primary α'-plate.

the corresponding BF-TEM image observed from an area including $\{1\,0\,\bar{1}\,1\}$-type twins. Reflections related to twins are marked by arrowheads in the SAED pattern. Thin twin plates, 20–50 nm in thickness, can be seen in the BF-TEM image. The $\{1\,0\,\bar{1}\,1\}$ twin is typically observed in quenched Ti–V alloys with a hexagonal α' martensite structure [5,11]. Therefore, it is noted that the $\{1\,0\,\bar{1}\,1\}$-type twins formed by martensitic transformation still remain in this alloy after aging at 400 °C for 24 h, in accordance with the results by XRD shown in Fig. 1b. This observation also suggests that the martensitic reverse transformation temperature of this alloy is higher than 400 °C. Fig. 4c is an HRTEM image, showing a thin twin band with thickness of 18 nm at the atomic level, where two twin boundaries are indicated by arrows. A magnified image is shown in the inset. As seen here, the twin boundaries are free from precipitates or stacking faults in spite of substantial age-hardening. However, local Moiré fringes can be observed at the twin boundaries, indicating superposition of small crystallites with a slightly different orientation at the boundary region.

To further clarify possible evolution of the retained β phase on aging at 400 °C, we employed dark-field (DF) TEM imaging for the area including the β phase. Fig. 5a shows an SAED pattern with a beam incidence of $[0\,0\,1]_\beta$, which shows reflections from α' martensites. Single- and double-arrowheads indicate $0\,0\,0\,1_{\alpha'}$

reflections belonging to different variants. The OR between β and α' is the same as that observed in Fig. 2b. Fig. 5b is a DF-TEM image taken with $\bar{1}\,1\,0_\beta$ reflection, showing fine precipitates, 10–100 nm in sizes, inside the α' plates. It should be mentioned here, however that, since the $\bar{1}\,1\,0_\beta$ reflection coincides with $0\,0\,0\,\bar{2}_{\alpha'}$ and $\bar{1}\,0\,1\,0_{\alpha'}$ reflections, bright contrasts in Fig. 5b are not only those arising from the precipitated β phase but also those from primary α' crystals. To clarify detailed morphologies inside the aged α' crystals, and possible partitioning of elements, we employed Z contrast imaging of HAADF-STEM. Fig. 5c shows a HAADF-STEM image of the alloy aged at 400 °C for 24 h. A high magnification image is also shown in Fig. 5d. Here, fine acicular precipitates, ~50 nm in length, can clearly be seen as bright contrasts inside the primary α' plates. Because of the incoherent nature of the Z contrast imaging, fine morphologies observed here correspond to the precipitated β phase, in which presumably vanadium atoms are enriched. Thus, the age-hardening observed in this alloy can be attributed to these high-density fine β precipitates inside the primary α' plate. It is known that hardness of Ti-alloys is largely affected by the addition of carbon [20,21], nitrogen [22], and/or oxygen [23]. Here, in this study, the contents of C, N, O in an STQ alloy were 0.025, 0.009, and 0.104 mass%, respectively, which are much lower than those reported previously. For example, significant effects on hard-
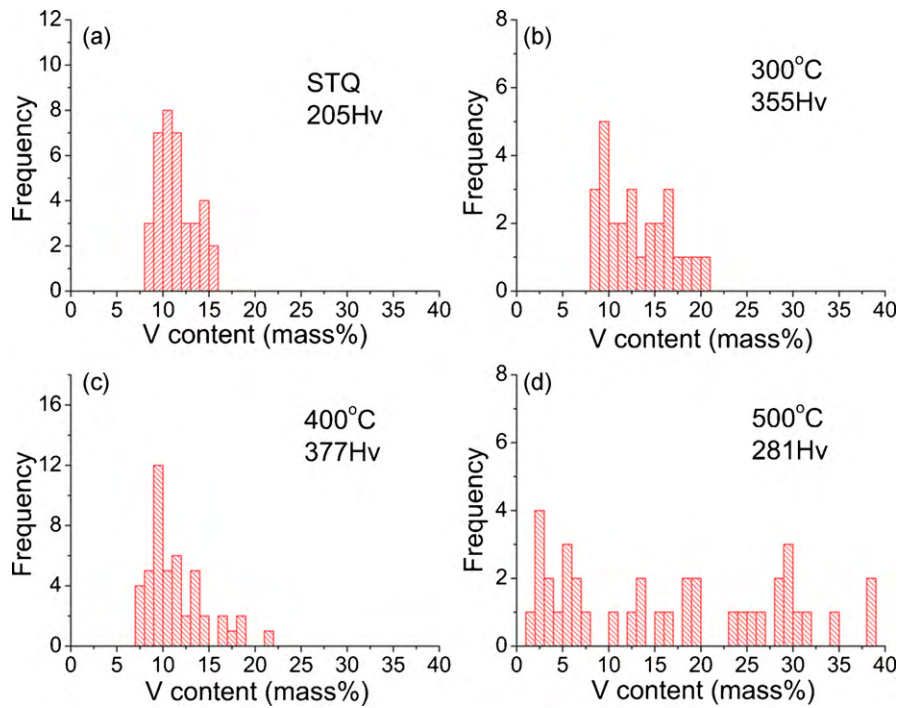
Fig. 6. Summary of STEM-EDS elemental analyses for a STQ and aged alloys. The statistical errors are as follows: Ti–K ($\approx$1%), V–K (1–4%), Al–K (2–7%). The aging conditions are 300 °C for 500 h (3 weeks), 400 °C for 24 h, and 500 °C for 24 h. As aging proceeds at 300–400 °C, the spread of the distribution of vanadium content becomes wider, indicating the initiation of phase decomposition towards the equilibrium α and β phases. At 500 °C, the re-distribution of vanadium is evident.

ness by an addition of 0.1%C, 0.6%N, and 0.2–0.4%O have been described in Refs. [20–23], respectively. Thus, the effects of these elements on age-hardening can be excluded in this study, but we may attribute the observed increase in hardness to the changes in microstructure.

3.2. Distribution of solute vanadium and its evolution on aging

As seen in the DF-TEM and HAADF-STEM images, precipitation of the fine β plates occurs inside the α' martensites during aging. Such β precipitates are expected to be enriched in vana-

dium according to the binary phase diagram, which was found also in accordance with the HAADF-STEM image in Fig. 5c. To check possible compositional variations in a more quantitative manner, we have carried out STEM-EDS elemental analyses. Fig. 6 summarizes the results of STEM-EDS for as-quenched and aged alloys. In this experiment, we measured V contents from randomly chosen areas (37, 27, 47, and 38 points for STQ, 300, 400, and 500 °C-annealed specimens, respectively), and plotted the frequency of occurrence against the V content. Fig. 6a, which is the result of the STQ alloy, shows that the measured vanadium content ranged from 8 to 16 mass%. We can estimate a statistical error of the inte-
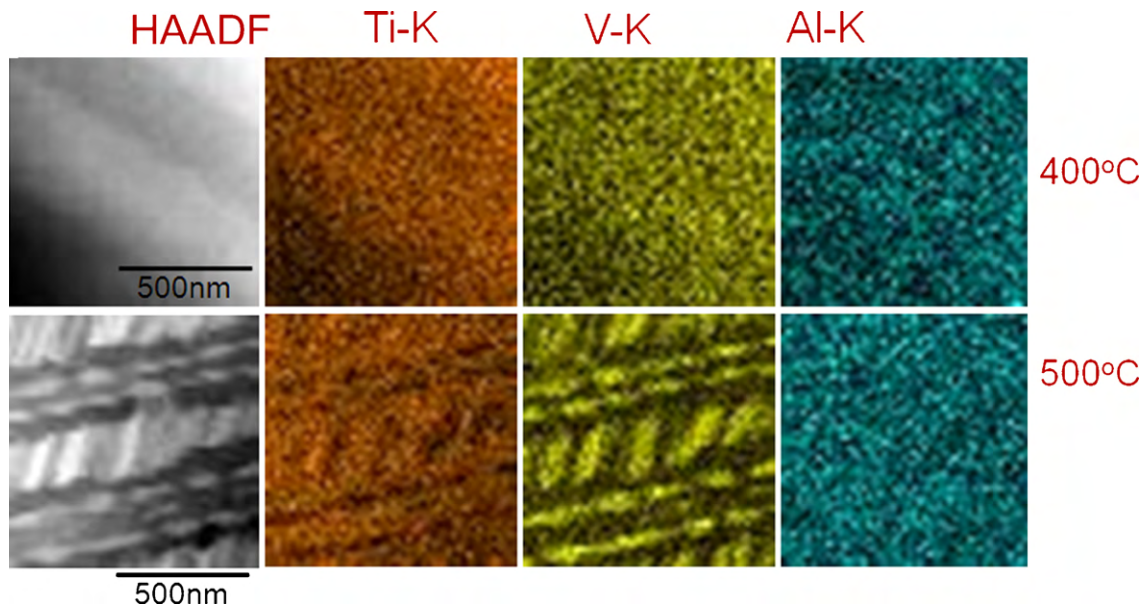

Fig. 7. STEM-EDS elemental mapping for alloys after aging at 400 °C for 24 h, and 500 °C for 24 h. The pixel size is 19.3 nm. Partitioning of atoms upon the decomposition of the α' martensite was detected for the alloy after aging at 500 °C. Bright region in the HAADF-STEM image corresponds to the vanadium-rich β precipitates.

grated intensity of V–K characteristic X-ray ($\sqrt{N}/N$, N: integrated intensity) to be at most ±4% within the present experimental condition. After aging at 300 °C for 3 weeks, spread of the distribution became 12% (Fig. 6b), and it further increased to 14% after aging at 400 °C for 24 h (Fig. 6c). These distributions are broader than the aforementioned statistical error by 4–6%, and the V content reaches as high as 20 mass%, which is 8% higher than the average alloy composition (12 mass%). Thus, the re-distribution of V atoms on aging has been confirmed by the present STEM-EDS analyses, which, in return, suggests that fine β phase particles precipitated during age-hardening between 300 and 400 °C (Fig. 3a and b).

After aging at 500 °C for 24 h, the distribution of V content broadens further as shown in Fig. 6d: for example, the observed maximum V content in the β phase was as high as 38 mass%. This finding suggests that the α′ martensite plates decomposed into the equilibrium V-deficient α and V-rich β phases. This phase separation behavior is also in accordance with the results of XRD shown in Fig. 1c. Namely, the degradation of mechanical property is associated with such phase decomposition and the hardness abruptly dropped to 281 Hv (Fig. 3b).

We investigated the partitioning of elements upon decomposition using STEM-EDS elemental mapping for the specimens annealed at 400 and 500 °C, as shown in Fig. 7. First, STEM-EDS maps for the alloy after aging at 400 °C does not show any fine details at this resolution, in spite of the existence of fine precipitates, probably due to a large pixel size of 19.3 nm/pixel. In contrast, the decomposed α/β two-phase structure in the alloy after aging at 500 °C for 24 h is clearly seen. Here, the bright contrast region seen in the HAADF-STEM image corresponds to the V-rich region in the V–K map. The Al–K maps does not show any details for both alloys since the Al-content is only 2 mass%, which is too small to be efficiently detected by STEM-EDS mapping.

Fig. 8a shows HAADF-STEM image of the decomposed α/β two-phase structure obtained after the 500 °C annealing. The bright and the dark contrast regions correspond to the β and α phases, respectively. This image shows that the primary α′ phase decomposed into the two phases with distinct morphology, exhibiting clear habit planes. HRTEM image of the α/β interface is shown in Fig. 8b. The upper left corner of the image corresponds to [1 0 $\bar{1}$ 1] zone of the α phase, while the right hand side shows crossed {1 1 0} lattice fringes of the β phase with [0 1 0] zone. The interface deduced from the bending of the lattice fringes is indicated in the image. Moiré fringes can also be seen in the image, indicating superposition of these two crystals near the boundary. Fig. 8c and d shows magnified images of these two crystals. By analyzing Fourier spectra of these two regions as well as the lattice fringes, the angles between $(\bar{1}\,1\,0\,1)_\alpha$ and $(\bar{1}\,0\,1)_\beta$ was estimated to be about 7–8°, which is close to 9.3°, the value predicted by the Burgers' OR [24]. The HRTEM image also shows a relation, $(0\,1\,\bar{1}\,\bar{1})_\alpha \| (1\,0\,1)_\beta$. Therefore, it can be considered that the β precipitate grows parallel to the primary {1 0 $\bar{1}$ 1}-type twin plates. These observations indicate a good lattice correspondence exist between the hexagonal α and the cubic β phases.

3.3. Three-dimensional structures of β-precipitates viewed by electron tomography

We have examined 3D morphology of the decomposed α/β two-phase structure of the specimen after aging for 24 h at 500 °C by means of a tomographic technique based on a series of HAADF-STEM images. In electron tomography, 3D structures can be reconstructed from a tilt-series data set of 2D images having Z contrasts. In the present study, we set the inner half angle of the HAADF detector to be 30 mrad to ensure a clear contrast during the tilt-series acquisition. This setting of a rather low angle may
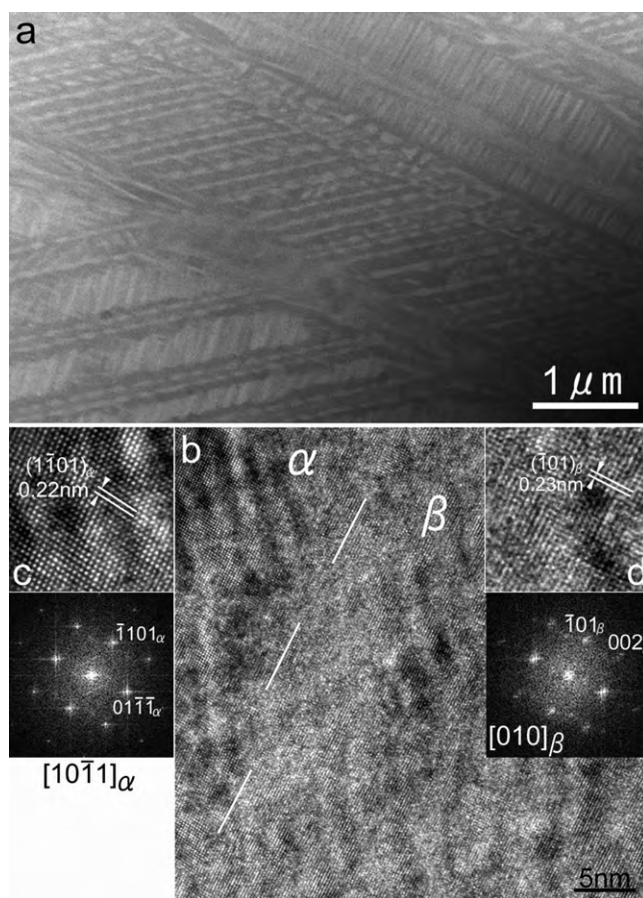

Fig. 8. Microstructure of the two-phase structure after aging at 500 °C for 24 h. (a) HAADF-STEM image. (b) Aberration-corrected HRTEM image at the α/β interface region. The interface is not obvious and several Moiré fringes are seen, indicating superposition of small crystallites at the interface region. (c and d) Magnified images and corresponding Fourier spectra for these α and β structures.

break the simple Z^2 dependence of the HAADF-STEM images to some extent due to possible diffraction contrasts during the tilting. The tilt-series was obtained sequentially from 0° to −70° and then 0° to +70°. The angular tilt angle increments were set 2°. Out of this data set, we employed images taken at tilt angles between −62° and +62° for subsequent 3D reconstruction. Fig. 9 shows one of the original images (Fig. 9a) and corresponding reconstructed images processed by WBP (Fig. 9b). Side-view projections (y–z and z–x) are also shown in Fig. 9b. Here, the x-axis is the tilt axis, about which the specimen film is sequentially tilted towards the y-direction; while the primary beam incidence direction is parallel to the z-axis. Because the original images are essentially Z contrast, bright region corresponds to the precipitated V-rich β phase. A bird-view of the reconstructed volume is shown in Fig. 9c. It can be said that in the present study using HAADF-STEM tomography, the plate-like 3D shapes of precipitated β phase has been successfully reconstructed. As seen in these images, general features projected onto the x–y plane, such as plate-like shape, size, and the location of precipitates, are clearly reconstructed. However, it is noted that floating dot-like artifacts are seen in the reconstructed volume, which can be attributed to a low signal to noise ratio and diffraction effects of the original tilt-series images.

Within the framework of single-axis tilt geometry, the resolution along x-, y-, and z-directions are all different. The resolution along the tilt axis (x-axis) is the resolution of the microscope and therefore highest resolution is expected in this direction. On the other hand, resolutions in the y- and z-directions are affected by the
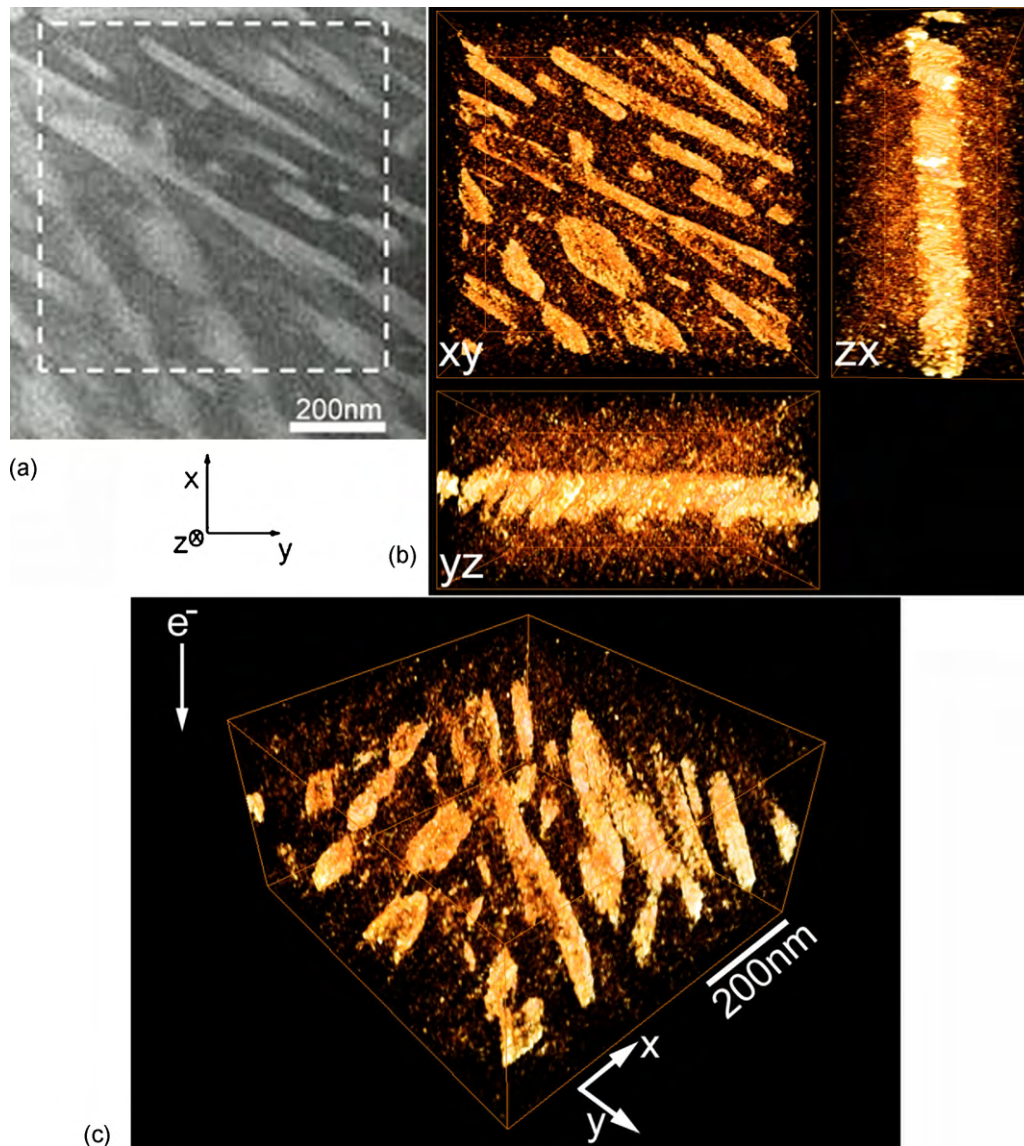
Fig. 9. 3D distribution of the β phase in the 500 °C-annealed specimen observed by HAADF-STEM tomography using a weighted back-projection (WBP) technique. (a) An original HAADF-STEM image. Bright regions correspond to the V-rich β phase. (b) Reconstructed images processed by WBP. (c) A bird-view of the reconstructed volume. The reconstructed volume is 690 nm × 720 nm × 375 nm. Plate-like structures correspond to the β precipitates. See text for estimated errors.

maximum tilt angle (α), the number of images used for reconstruction (N), and the diameter of the reconstructed volume assuming a cylindrical shape (D) [16,25]. In fact, the resolution along the y- and z-axes, d_y and d_z, respectively, are expressed as follows,

$$d_y = \frac{\pi D}{N} \tag{1}$$

$$d_z = d_y e_{yz} \tag{2}$$

$$e_{yz} = \sqrt{\frac{\alpha + \sin\alpha\cos\alpha}{\alpha - \sin\alpha\cos\alpha}} \tag{3}$$

where e_{yz} is the so-called elongation factor, which represents the effect of a missing data set (missing wedge) at high angles on reconstruction. Numerically, we can derive the resolution in the present study by applying experimental parameters ($N = 63$, $D = 720$ nm, $\alpha = 62°$), which yielded the following values: $d_y = 36$ nm, $d_z = 54$ nm, for the reconstructed volume (xyz) of 690 nm × 720 nm × 375 nm. These estimated errors, d_y and d_z, correspond to 5% and 14% of the y- and z-directions of the reconstructed volume, respectively. Note that Eq. (1) assumes the tilting range from −90° to 90° with an equal

angular increment. Hence it is only an approximation in the case of electron tomography, where tilting range is limited. In fact, according to our recent study on electron tomography [26], Eqs. (1)–(3) tend to overestimate the error of a reconstructed volume, especially along the z-axis. To reduce the artifacts and experimental errors, minimization of the missing wedge is most effective, which can be attained by increasing the maximum tilt angle together with number of 2D-slice images as possible. For more quantitative analyses of 3D structures of β precipitates, thus further experiments, including DF-TEM tomography [27] as well as in situ TEM observation [28], are necessary.

4. Summary

We have studied the microstructure and phase decomposition behaviors of the hexagonal α' martensite in Ti–12 mass%V–2 mass%Al alloys aged at temperatures between 300 and 500 °C by means of TEM, STEM and electron tomography. Main results are summarized as follows:

1. As-quenched alloy after solution treatment (STQ) showed the acicular structure of the hexagonal α' martensites with a small amount of the retained β phase. The following OR, close to the Burgers' OR, was observed between the retained β phase and the α' martensite: $(0\,0\,0\,1)_{\alpha'}||(1\,\bar{1}\,0)_{\beta}$, $[\bar{1}\,2\,\bar{1}\,0]_{\alpha'} \approx ||[0\,0\,1]_{\beta}$.

2. Significant age-hardening is associated with densely distributed fine acicular precipitates, about 50 nm in length, of the β phase nucleated inside the primary α' martensite plates.

3. As aging proceeds, re-distribution of vanadium becomes prominent, indicating a tendency of phase decomposition towards the equilibrium α and β phases. Vickers hardness abruptly dropped after the establishment of α/β two-phase structure.

4. The α' martensite phase was maintained up to 400 °C, while it completely decomposed into the α and β phases at 500 °C. The OR between the α and the β phases is close to the Burgers' OR, indicating a well-defined lattice correspondence.

5. Plate-like 3D shapes and distribution of large β precipitates have been reconstructed by means of HAADF-STEM tomography with weighted back-projection (WBP) technique.

Acknowledgments

References

[1] E.W. Collings, The Physical Metallurgy of Titanium Alloys, ASM, Metals Park, OH, 1984.
[2] G. Lutjering, J.C. Williams, Titanium, Springer, Berlin, 2003.
[3] M. Niinomi, Metall. Mater. Trans. A 33A (2002) 477–486.
[4] H. Matsumoto, S. Watanabe, N. Masahashi, S. Hanada, Metall. Mater. Trans. A 37A (2006) 3239–3249.
[5] H. Matsumoto, S. Watanabe, S. Hanada, Mater. Sci. Eng. A 448 (2007) 39–48.
[6] H. Matsumoto, K. Kodaira, A. Chiba, J. Jpn. Inst. Met. 72 (2008) 989–996.
[7] H. Matsumoto, K. Kodaira, K. Sato, T.J. Konno, A. Chiba, Mater. Trans. 50 (2009) 2744–2750.
[8] H.K. Adenstedt, J.R. Pequignot, J.M. Raymer, Trans. ASM 44 (1952) 990–1003.
[9] F.R. Brotzen, E.L. Harmon Jr., A.R. Troiano, Trans. TMS-AIME 203 (1955) 413–419.
[10] H.M. Flower, R. Davis, D.R.F. West, in: J.C. Williams, A.F. Belov (Eds.), Titanium and Titanium Alloys, Scientific and Technological Aspects (Proc. Third Int. Conf. on Titanium, Moscow), Plenum Press, New York, 1982, pp. 1703–1715.
[11] R. Davis, H.M. Flower, D.R.F. West, Acta Metall. 27 (1979) 1041–1052.
[12] H. Okamoto, J. Phase Equilibr. 14 (1993) 266–267.
[13] M. Hansen, Constitution of Binary Alloys, 2nd ed., McGraw-Hill, New York, 1958, pp. 976–978.
[14] M. Sluiter, P.E.A. Turchi, Phys. Rev. B 43 (1991) 12251–12266.
[15] K. Kodaira, Master's Thesis, Tohoku University, 2008.
[16] M. Radermacher, in: J. Frank (Ed.), Electron Tomography: Three-dimensional Imaging with the Transmission Electron Microscope, Plenum Press, New York, 1992, pp. 91–115.
[17] J.C. McMillan, R. Taggart, D.H. Polonis, Trans. Met. Soc. AIME 239 (1967) 739–742.
[18] J.C. Williams, M.J. Blackburn, Trans. ASM 60 (1967) 373–383.
[19] J.C. Williams, in: R.I. Jaffee, H.M. Burte (Eds.), Titanium Science and Technology (Proc. Second Int. Conf. on Titanium, Boston), Plenum Press, New York, 1973, pp. 1443–1494.
[20] X. Wu, J. del Prado, Q. Li, A. Huang, D. Hu, M.H. Loretto, Acta Mater. 54 (2006) 5433–5448.
[21] T. Furuhara, S. Annaka, T. Maki, J. Jpn. Inst. Met. 72 (2008) 942–948.
[22] T. Ando, K. Nakashima, T. Tsuchiyama, S. Takaki, Mater. Sci. Eng. A 486 (2008) 228–234.
[23] M. Nakai, M. Niinomi, T. Akahori, H. Ishikawa, M. Ogawa, J. Jpn. Inst. Met. 72 (2008) 960–964.
[24] T. Furuhara, T. Makino, Y. Idei, H. Ishigaki, A. Takada, T. Maki, Mater. Trans. JIM 39 (1998) 31–39.
[25] P.A. Midgley, M. Weyland, Ultramicrosc 96 (2003) 413–431.
[26] K. Sato, K. Aoyagi, T.J. Konno, J. Appl. Phys. 107 (2010), 024304.
[27] K. Kimura, S. Hata, S. Matsumura, T. Horiuchi, J. Electron Microsc. 54 (2005) 373–377.
[28] S. Semboshi, T. Shirai, T.J. Konno, S. Hanada, Metall. Mater. Trans. A 37A (2008) 2820–2829.